

PRD Rapid Communication Draft v4.0  
Authors: M. Martinez  
(IFAE-Barcelona)

**Study of Jet Shapes**  
**in Inclusive Jet Production in p anti-p Collisions at  $\sqrt{s} = 1.96$  TeV**  
(The CDF Collaboration)

We report on a study of jet shapes in inclusive jet production in  $p\bar{p}$  collisions at  $\sqrt{s} = 1.96$  TeV using the upgraded Collider Detector at Fermilab in Run II (CDF II) and based on an integrated luminosity of  $170 \text{ pb}^{-1}$ . Measurements are performed for jets with rapidity  $0.1 < |Y^{\text{jet}}| < 0.7$  and transverse momentum  $37 \text{ GeV}/c < P_T^{\text{jet}} < 380 \text{ GeV}/c$  and are corrected to the hadron level. The measured jet shapes are compared to leading-order QCD parton-shower Monte Carlo predictions as implemented in Pythia and Herwig programs. The current CDF tuning of Pythia performs better than the default Herwig.

PACS numbers: Need PACS numbers

## I. INTRODUCTION

The measurement of the jet shape [1] allows to study the transition between a parton produced in a hard process and the collimated flow of hadrons observed experimentally. The internal structure of jets is dominated by multi-gluon emissions from the primary parton and it is expected to depend mainly on the type of parton, quark or gluon, in the final state. In hadron-hadron collisions, the jet shape also receives contributions from soft-gluon initial-state radiation and multiple parton interactions between remnants (so-called *underlying event*) which are only described in terms of phenomenological models. The comparison of jet cross section measurements with perturbative QCD predictions as well as the estimation of QCD backgrounds in the search for new physics require an accurate description of the underlying event. The study of jet shapes at the Tevatron provides a precise mean to test the validity of the models for parton cascades and soft-gluon emissions in hadron-hadron collisions. Measurements of the jet shape have been performed in  $p\bar{p}$  collisions at  $\sqrt{s} = 1.8$  TeV [2], deeply inelastic scattering (DIS) [3] and photoproduction [4] processes in  $e^\pm p$  collisions at HERA, and  $e^+e^-$  interactions at LEP1 [5]. It was observed [5] that the jets in  $p\bar{p}$  collisions are significantly broader than those in  $e^+e^-$  and most of the difference was explained in terms of the different mixtures of quark and gluon jets in the final state. The jets in DIS were found to be very similar to those in  $e^+e^-$  interactions and narrower than those in  $p\bar{p}$  collisions. In this paper, new jet shape results in  $p\bar{p}$  collisions, based on CDF Run II data, are presented for central jets in a wide region in jet transverse momentum. For the first time, these measurements extend the study of the jet internal structure to jets with transverse momentum up to 380 GeV/c.

## II. EXPERIMENTAL SETUP

The CDF II detector is described in detail in [6]. In this section, the sub-detectors most relevant for this analysis are briefly discussed. As illustrated in Fig. 1, the detector has a charged particle tracking system immersed in a 1.4 T magnetic field, aligned coaxially with the beam line. A silicon microstrip detector [7] provides tracking over the radial range 1.35 to 28 cm. A 3.1 m long open-cell drift chamber, the Central Outer Tracker (COT) [8], covers the radial range from 44 to 132 cm. The fiducial region of the silicon detector covers the pseudorapidity [9] range  $|\eta| \sim 2$ , while the COT provides coverage for  $|\eta| \leq 1$ . The charged particles are reconstructed in the COT with a transverse-momentum resolution of  $\sigma/p_T^2 \sim 1.7 \cdot 10^{-3} [\text{GeV}/c]^{-1}$ . Segmented sampling calorimeters, arranged in a projective tower geometry, surround the tracking system and measure the energy flow of interacting particles in  $|\eta| \leq 3.6$ . The CDF central barrel calorimeter [10] is unchanged from Run I and covers the region  $|\eta| < 1$ . It is constituted by an electromagnetic (CEM) calorimeter and an hadronic (CHA) calorimeter segmented into 480 towers of size 0.1 in  $\eta$  and  $15^\circ$  in  $\phi$ . The end-wall hadronic (WHA) calorimeter [11] complements the coverage of the central barrel calorimeter in the region  $0.6 < |\eta| < 1.0$  and provides additional forward coverage out to  $|\eta| < 1.3$ . In Run II, new forward scintillator plate calorimeters [12] replaced the original Run I gas calorimeter system. The new plug electromagnetic (PEM) calorimeter covers the region  $1.1 < |\eta| < 3.6$  while the new hadronic (PHA) calorimeter provides coverage in the  $1.3 < |\eta| < 3.6$  region. Each end plate calorimeter is segmented into 480 towers with sizes that vary as a function of  $\eta$  (0.1 in  $\eta$  and  $7.5^\circ$  in  $\phi$  at  $|\eta| = 1.1$  to 0.5 in  $\eta$  and  $15^\circ$  in  $\phi$  at  $|\eta| = 3.6$ ). The calorimeter presents a major crack at  $\eta = 0$  (between the two halves of the central barrel calorimeter) and two cracks at  $\eta = \pm 1.1$  (in the region between the WHA and the plug calorimeters). The measured energy resolutions for electrons in the electromagnetic calorimeters are  $14\%/\sqrt{E_T}$  (CEM) and  $16\%/\sqrt{E} + 1\%$  (PEM) where the units are expressed in GeV. The single-pion energy resolution in the hadronic calorimeters, as determined in test-beam data, are  $75\%/\sqrt{E_T}$  (CHA),  $80\%/\sqrt{E}$  (WHA) and  $80\%/\sqrt{E} + 5\%$  (PHA). Cherenkov counters located in the  $3.7 < |\eta| < 4.7$  region [13] measure the average number of inelastic  $p\bar{p}$  collisions per bunch crossing and thereby determine the beam luminosity. Finally, a three-level trigger system [14] is used to select events online, as described in section V.

## III. MONTE CARLO SIMULATION

Monte Carlo event samples are used to determine the response of the detector and the correction factors to the hadron level for the measured jet shapes. The generated samples are passed through a full CDF detector

simulation (based on GEANT 4 [15] where the GFLASH [16] package is used to simulate the particle showers in the calorimeters), and then reconstructed and analyzed using the same analysis chain as in the data. Samples of simulated inclusive jet events have been generated using the PYTHIA 6.203 [17] and HERWIG 6.4 [18] Monte Carlo generators. In both programs, the partonic interactions are generated using leading-order QCD matrix elements, including initial and final parton showers. CTEQ5L [19] parton distribution functions are used for the proton and antiproton. The HERWIG samples have been generated using default parameters. The PYTHIA samples have been created using a special tuned set of parameters (denoted as PYTHIA-Tune A [20]) that control soft-gluon emissions in the initial and final state. Tune A was determined as a result of dedicated studies of the underlying event performed using CDF Run I data [21]. In addition, two different PYTHIA samples have been generated using default parameters with and without the contribution from multiple parton interactions (MPI) between proton and antiproton remnants, the latter denoted as PYTHIA-(no MPI). The HERWIG samples do not include multiple parton interactions. Fragmentation into hadrons is carried out using the string model [22] as implemented in JETSET [23] in the case of PYTHIA and the cluster model [24] in HERWIG.

#### IV. JET RECONSTRUCTION

An iterative cone-based midpoint algorithm [25] in the  $Y$ - $\phi$  plane [9] is used to reconstruct jets from the energy deposits in the calorimeter towers for both data and Monte Carlo simulated events and from final-state particles (hadrons) for Monte Carlo generated events. The procedure is explained in detail for the jet reconstruction from the calorimeter towers. In a first step, the electromagnetic and hadronic sections of each calorimeter tower are preclustered into a *physics* tower. The position of each section is determined from the unit vector joining the vertex of the interaction and its geometrical center and each section is assumed to be massless. The four-vector components of each physics tower are then computed using the four-momentum sum of its electromagnetic and hadronic sections, and only towers with transverse momentum above 0.1 GeV/c are further considered. In a second step, each physics tower with transverse momentum above 1 GeV/c defines a seed for the jet search. Starting from the seed with highest transverse momentum, a cone is drawn around each seed and the physics towers inside a distance  $\sqrt{(\Delta Y)^2 + (\Delta\phi)^2} < R/2$ , with  $R = 0.7$  are used to determine the direction of the new cluster as indicated in Eqs. 1 and 2:

$$E^{\text{cluster}} = \sum_{\text{phys.towers}} E^{\text{tower}}, \quad P_i^{\text{cluster}} = \sum_{\text{phys.towers}} P_i^{\text{tower}} \quad i = x, y, z \quad (1)$$

$$P_T^{\text{cluster}} = \sqrt{(P_x^{\text{cluster}})^2 + (P_y^{\text{cluster}})^2}, \quad Y^{\text{cluster}} = \frac{1}{2} \frac{E^{\text{cluster}} + P_z^{\text{cluster}}}{E^{\text{cluster}} - P_z^{\text{cluster}}}, \quad \phi^{\text{cluster}} = \tan^{-1}\left(\frac{P_y^{\text{cluster}}}{P_x^{\text{cluster}}}\right) \quad (2)$$

where  $Y^{\text{cluster}}$  and  $\phi^{\text{cluster}}$  denote the rapidity and azimuthal angle of the cluster, respectively. Starting from the list of resulting clusters, the procedure is iterated until the contents of the clusters remain unchanged. In a third step, the midpoint ( $Y$ - $\phi$  plane) between each pair of stable clusters separated by less than  $2R$  is added to the list of clusters. The clustering algorithm, as explained above, is again iterated until stability is achieved. This latter step gives the name to the jet algorithm and it was introduced in order to address the theoretical difficulties [26] of the cone-based jet algorithm used in Run I [27]. Finally, the momentum sharing of overlapping clusters is considered. Overlapping jets are merged if their shared momentum is larger than 75% of the jet with smaller transverse momentum; otherwise two jets are formed and the common towers are assigned to the nearest jet. The variables of jets reconstructed from the calorimeter towers are denoted by  $P_{T,\text{CAL}}^{\text{jet}}$ ,  $Y_{\text{CAL}}^{\text{jet}}$  and  $\phi_{\text{CAL}}^{\text{jet}}$ . As mentioned, the same jet algorithm is applied to the final-state hadrons in Monte Carlo generated events. The variables of the hadron-level jets are denoted by  $P_{T,\text{HAD}}^{\text{jet}}$ ,  $Y_{\text{HAD}}^{\text{jet}}$  and  $\phi_{\text{HAD}}^{\text{jet}}$ .

The reconstruction of the jet variables in the calorimeter is studied using Monte Carlo event samples and matched pair of jets at the calorimeter and hadron levels. These studies indicate that the angular variables of the jet,  $Y_{\text{CAL}}^{\text{jet}}$  and  $\phi_{\text{CAL}}^{\text{jet}}$ , are reconstructed in the calorimeter with no significant shift and with a resolution, for jets with  $P_{T,\text{CAL}}^{\text{jet}} > 20$  GeV/c, of the order of 0.02 units and 0.025 units, respectively. The resolutions

improve as the measured jet transverse momentum increases. The jet transverse momentum measured in the calorimeter,  $P_{T,CAL}^{jet}$ , systematically underestimates that of the hadron level jet. This is mainly due to the non-compensating nature of the calorimeter [28]. For jets with  $P_{T,CAL}^{jet} > 20$  GeV/c the jet transverse momentum is reconstructed with an average shift of  $-20\%$  and an r.m.s of  $17\%$ . The reconstruction of the jet transverse momentum improves as  $P_{T,CAL}^{jet}$  increases. For jets with  $P_{T,CAL}^{jet} > 130$  GeV/c the jet transverse momentum is reconstructed with an average shift of  $-12\%$  and an r.m.s of  $9\%$ . An average correction is extracted from the Monte Carlo using the following procedure: matched pairs of jets are used to study the difference between the jet transverse momentum at the hadron level,  $P_{T,HAD}^{jet}$ , and the corresponding measurement in the calorimeter,  $P_{T,CAL}^{jet}$ . The resulting correlation is used to extract multiplicative correction factors,  $C(P_{T,CAL}^{jet})$ , which are then applied to the measured jets to obtain the corrected jet transverse momenta,  $P_{T,COR}^{jet} = C \times P_{T,CAL}^{jet}$  [29].

## V. EVENT SELECTION

This analysis is based on a sample of inclusive jet events selected from the CDF Run II data corresponding to a total integrated luminosity of  $170 \text{ pb}^{-1}$ . Events were collected online using three-level trigger paths, based on the measured energy deposits in the calorimeter towers, with several different thresholds on the jet transverse energies (see Table I). In the first-level trigger, a single trigger tower with transverse energy above 5 GeV or 10 GeV (depending on the trigger path) is required. In the second-level trigger, a hardware-based clustering is carried out where calorimeter clusters are formed around the selected trigger towers. The events are required to have at least one second-level trigger cluster with transverse energy above a given threshold. In the third-level trigger, jets are reconstructed using the CDF Run I cone algorithm [27] and the events are required to have at least one jet with transverse energy above threshold.

Trigger Name	Level 1	Level 2	Level 3	$P_{T,COR}^{jet}$ range (GeV/c)
Single tower 5 GeV	5 GeV	-	-	37 - 55
Jet 20 GeV	5 GeV	15 GeV	20 GeV	55 - 84
Jet 50 GeV	5 GeV	40 GeV	50 GeV	84 - 112
Jet 70 GeV	10 GeV	60 GeV	70 GeV	112 - 166
Jet 100 GeV	10 GeV	90 GeV	100 GeV	166 - 380

TABLE I: Details of the three-level trigger configurations and energy thresholds used in the analysis for the different regions in  $P_{T,COR}^{jet}$ . The corresponding  $P_{T,COR}^{jet}$  ranges are such that the relevant trigger path is always 100% efficient.

Offline, jets are reconstructed using the midpoint algorithm, as explained above, starting from seed calorimeter towers with transverse momentum above 1 GeV/c and only considering towers with a minimum transverse momentum of 100 MeV/c in the clustering procedure. The following selection criteria have been imposed:

- One reconstructed primary vertex with z-component,  $V_Z$ , in the region  $|V_Z| < 60$  cm. Events with more than one primary vertex are removed to eliminate contributions from pile-up events with multiple proton-antiproton interactions per beam crossing. The data used in this study was collected at Tevatron instantaneous luminosities in the range between  $0.2 \times 10^{31} \text{ cm}^{-2} \text{ s}^{-1}$  and  $4 \times 10^{31} \text{ cm}^{-2} \text{ s}^{-1}$  for which, in average, less than one interaction per crossing is expected.
- $E_T/\sqrt{E_T} < 3.5 \text{ GeV}^{-1/2}$ , where  $E_T$  ( $E_T$ ) denotes the missing (total) transverse energy of the event as determined from the energy deposits in the calorimeter towers. This cut eliminates beam-related backgrounds (beam halo and beam-gas contributions) and cosmic rays.
- At least one jet with  $P_{T,COR}^{jet} > 37 \text{ GeV/c}$  and  $Y^{jet}$  in the region  $0.1 < |Y^{jet}| < 0.7$ .

The cut on the minimum  $P_{T,COR}^{jet}$  is dictated by the trigger. In order to avoid any possible bias on the measured jet shapes due to the three-level trigger selection, the thresholds on  $P_{T,COR}^{jet}$  have been selected such that the

trigger is fully efficient in the whole kinematic region under study. The measurements are performed for central jets in a rapidity region away from calorimeter cracks and well inside the fiducial region of the CDF tracking system.

## VI. JET SHAPE

### A. Jet shape definition

The differential jet shape as a function of the distance  $r = \sqrt{\Delta Y^2 + \Delta \phi^2}$  to the jet axis,  $\rho(r)$ , is defined as the average fraction of the jet transverse momentum that lies inside an annulus of inner radius  $r - \delta r/2$  and outer radius  $r + \delta r/2$  around the jet:

$$\rho(r) = \frac{1}{\delta r} \frac{1}{N_{\text{jet}}} \sum_{\text{jets}} \frac{P_T(r - \delta r/2, r + \delta r/2)}{P_T(0, R)}, \quad 0 \leq r \leq R \quad (3)$$

where  $N_{\text{jet}}$  denotes the total number of jets,  $P_T(r - \delta r/2, r + \delta r/2)$  is the transverse momentum within an annulus and the jet shape is determined for values of  $r$  between 0.05 and 0.65 using  $\delta r = 0.1$  intervals. The points from the differential jet shape at different  $r$  values are correlated since, by definition,  $\int_0^R \rho(r) \delta r = 1$ .

The integrated jet shape,  $\Psi(r)$ , is defined as the average fraction of the jet transverse momentum that lies inside a cone of radius  $r$  concentric to the jet cone:

$$\Psi(r) = \frac{1}{N_{\text{jet}}} \sum_{\text{jets}} \frac{P_T(0, r)}{P_T(0, R)}, \quad 0 \leq r \leq R \quad (4)$$

where, by definition,  $\Psi(r = R) = 1$ . The integrated jet shape is determined in intervals  $\delta r = 0.1$  between  $r = 0$  and  $r = 0.7$  and the points at different  $r$  values are strongly correlated.

### B. Jet shape reconstruction

Calorimeter towers are used for both data and Monte Carlo simulated events to reconstruct the differential jet shape. For each jet, the scalar sum of the transverse momentum of the calorimeter towers assigned to it,  $P_T(r - \delta r/2, r + \delta r/2)$ , with a distance to the jet axis  $r' = \sqrt{(Y^{\text{tower}} - Y^{\text{jet}})^2 + (\phi^{\text{tower}} - \phi^{\text{jet}})^2}$  between  $r - \delta r/2$  and  $r + \delta r/2$ , is determined and divided by  $P_T(0, R)$ . The differential jet shape,  $\rho^{\text{CAL}}(r)$ , is then determined following the prescription in Eq. 1. Similarly, the integrated jet shape,  $\Psi^{\text{CAL}}(r)$ , is reconstructed using the calorimeter towers as defined in Eq. 2. The same procedure is applied to the final-state particles in Monte Carlo generated events to reconstruct the differential and integrated jet shapes at the hadron level,  $\rho_{\text{MC}}^{\text{HAD}}(r)$  and  $\Psi_{\text{MC}}^{\text{HAD}}(r)$ , respectively. For the latter no grid in the  $(Y-\phi)$  space has been used.

### C. Jet shape using charged particles

The CDF tracking system provides an alternative method to measure the shape of the jets using charged particles. For each jet, tracks with transverse momentum,  $p_T^{\text{track}}$ , above 0.5 GeV and pseudorapidity,  $\eta^{\text{track}}$ , in the region  $|\eta^{\text{track}}| < 1.4$  are assigned to it if their distances,  $r$ , with respect to the jet axis are smaller than 0.7, and the tracks are within 2 cm around the z-position of the primary vertex. The differential and integrated jet shapes,  $\rho^{\text{TRKS}}(r)$  and  $\Psi^{\text{TRKS}}(r)$ , are reconstructed following Eqs. 1 and 2 where the tracks assigned to each jet are used. The measured jet shapes using tracks are employed to study systematic uncertainties on the central measurements as determined using calorimeter towers (see next section). Therefore, detailed studies have been performed on track reconstruction efficiency inside jets as a function of  $r$  and the jet and track transverse momenta, for both data and Monte Carlo simulated events, using track embedding techniques [30].

The difference between efficiencies in the data and Monte Carlo are about 3% and approximately independent of  $r$  for tracks with  $0.5 < p_T^{\text{track}} < 2.0$  GeV. For tracks with  $p_T^{\text{track}} > 2.0$  GeV, the difference in efficiency is of the order of 5% at the core of the jet, and it decreases as  $r$  increases up to  $r = 0.5$  from where no difference is observed. The effect on the reconstructed jet shapes is smaller than 0.5% and thus has been absorbed into the systematic error.

## VII. UNFOLDING AND SYSTEMATIC STUDIES

The measured jet shapes, as determined using calorimeter towers, are corrected back to the hadron level using Monte Carlo samples of generated events. PYTHIA-Tune A provides a good description of the measured jet shapes in all regions of  $P_T^{\text{jet}}$  and is used to determine the correction factors in the unfolding procedure.

### A. Jet shape corrections

The measured jet shapes are corrected for acceptance and smearing effects back to the hadron level. The correction factors also account for the efficiency of the selection criteria and for jet reconstruction in the calorimeter. Differential and integrated jet shapes are reconstructed with Monte Carlo samples using both calorimeter towers,  $\rho_{\text{MC}}^{\text{CAL}}(r)$  and  $\Psi_{\text{MC}}^{\text{CAL}}(r)$ , and final-state hadrons,  $\rho_{\text{MC}}^{\text{HAD}}(r)$  and  $\Psi_{\text{MC}}^{\text{HAD}}(r)$ , in different regions of  $P_{T,\text{COR}}^{\text{jet}}$  and  $P_{T,\text{HAD}}^{\text{jet}}$ , respectively. Correction factors, defined as  $D(r) = \rho_{\text{MC}}^{\text{HAD}}(r)/\rho_{\text{MC}}^{\text{CAL}}(r)$  and  $I(r) = \Psi_{\text{MC}}^{\text{HAD}}(r)/\Psi_{\text{MC}}^{\text{CAL}}(r)$ , are then computed separately in each bin of  $P_{T,\text{COR}}^{\text{jet}}$ . The corrected differential and integrated measurements are determined from the measured jet shapes as  $\rho(r) = D(r) \cdot \rho^{\text{CAL}}(r)$  and  $\Psi(r) = I(r) \cdot \Psi^{\text{CAL}}(r)$ . The correction factors  $D(r)$  do not show a significant dependence on  $P_T^{\text{jet}}$  and vary between 1.2 and 0.9 as  $r$  increases. For the integrated jet shapes, the correction factors  $I(r)$  differ from unity by less than 10% for  $r > 0.2$ .

### B. Systematic uncertainties

A detailed study of the different sources of systematic uncertainties on the measured jet shapes has been performed [29]:

- The measured jet transverse momentum has been varied by  $\pm 5\%$  in the data to account for the uncertainty on the determination of the absolute energy scale in the calorimeter. The effect on the measured jet shapes is typically of the order of 2%.
- The unfolding procedure has been repeated using bin-by-bin correction factors extracted from HERWIG instead of PYTHIA-Tune A to account for any possible dependence on the modeling of parton cascades. The effect on the measured jet shapes is typically about 2% to 5%.
- The ratios of uncorrected jet shape measurements as determined using calorimeter towers and tracks,  $\rho^{\text{CAL}}(r)/\rho^{\text{TRKS}}(r)$  and  $\Psi^{\text{CAL}}(r)/\Psi^{\text{TRKS}}(r)$ , are compared between data and Monte Carlo simulated events. The deviations from unity observed in the data/Monte Carlo double ratio, typically below 5% for the whole  $P_T^{\text{jet}}$  range, are included in the systematic errors to account for the uncertainty on the description of the inactive material in front of the calorimeter and its response to low-energy particles.
- The measurements are performed in different regions of Tevatron instantaneous luminosity (between  $0.2 \cdot 10^{31} \text{ cm}^{-2}\text{s}^{-1}$  and  $4 \cdot 10^{31} \text{ cm}^{-2}\text{s}^{-1}$ ) to account for possible remaining contributions from pile-up events. No significant effect is found.

The total systematic uncertainties on  $\rho(r)$  and  $\Psi(r)$  have been computed for the different  $r$  ranges by adding in quadrature the deviations from the central values. The statistical uncertainties are negligible compared to the systematic errors except for jets with  $P_T^{\text{jet}} > 300$  GeV for which the measurements are dominated by statistical fluctuations. The systematic uncertainties have been added in quadrature to the statistical errors

and the total uncertainties are shown in the figures. The total uncertainty in the different measured data points, for different  $P_T^{\text{jet}}$  and  $r$  ranges, typically varies between 5% to 10% except for jets with  $P_T^{\text{jet}} > 300$  GeV for which the total error is typically above 20%.

## VIII. RESULTS

The corrected differential and integrated jet shapes,  $\rho(r)$  and  $\Psi(r)$ , refer to midpoint jets at the hadron level with cone size  $R = 0.7$  in the region  $0.1 < |Y^{\text{jet}}| < 0.7$  and  $37 \text{ GeV} < P_T^{\text{jet}} < 380 \text{ GeV}$ .

### A. Comparison with Monte Carlo

Figures 2 and 3 show the measured differential jet shapes,  $\rho(r/R)$ , as a function of  $P_T^{\text{jet}}$  for jets in the region  $0.1 < |Y^{\text{jet}}| < 0.7$  and  $37 \text{ GeV} < P_T^{\text{jet}} < 380 \text{ GeV}$ , compared to PYTHIA-Tune A and HERWIG Monte Carlo predictions at the hadron level. The measured jet shapes show a prominent peak at low  $r$  which indicates that the majority of the jet momentum is concentrated at  $r/R < 0.2$ . At low  $P_T^{\text{jet}}$ , the fraction of transverse momentum at the core of the jet is about a factor of 6 times larger than that at the tail. This factor increases at higher  $P_T^{\text{jet}}$  and it is of the order of 100 for jets with  $P_T^{\text{jet}} > 340 \text{ GeV/c}$ . PYTHIA-Tune A provides a good description of the measured jet shapes in all regions of  $P_T^{\text{jet}}$ . The jets predicted by HERWIG follow the measurements but tend to be narrower than the data at low  $P_T^{\text{jet}}$ . The latter can be attributed to the absent of additional soft contributions from multiple parton interactions in HERWIG, which are particularly important at low  $P_T^{\text{jet}}$ .

Figures 4 and 5 present the measured integrated jet shapes,  $\Psi(r/R)$ , as a function of  $P_T^{\text{jet}}$ , for jets with  $0.1 < |Y^{\text{jet}}| < 0.7$  and  $37 < P_T^{\text{jet}} < 380 \text{ GeV}$ , compared to HERWIG, PYTHIA-Tune A, PYTHIA and PYTHIA-(no MPI) predictions, to illustrate the importance of a proper modeling of soft-gluon radiation in describing the measured jet shapes. In addition, Figure 6 shows, for a fixed radius  $r_0 = 0.3$  (approximately half size of the cone of the jet), the average fraction of the jet transverse momentum outside  $r = r_0$ ,  $1 - \Psi(r_0/R)$ , as a function of  $P_T^{\text{jet}}$  where the points are located at the weighted mean in each  $P_T^{\text{jet}}$  range. The measurements show that the fraction of jet transverse momentum inside a given fixed  $r_0/R$  increases ( $1 - \Psi(r_0/R)$  decreases) with  $P_T^{\text{jet}}$ , indicating that the jets become narrower as  $P_T^{\text{jet}}$  increases. PYTHIA with default parameters produces jets systematically narrower than the data in the whole region in  $P_T^{\text{jet}}$ . The contribution from secondary parton interactions between remnants to the predicted jet shapes (as shown by the difference between PYTHIA and PYTHIA-(no MPI) predictions) is important at low  $P_T^{\text{jet}}$ . PYTHIA-Tune A predictions, which include an enhanced contribution from initial-state soft gluon radiation and a tuned set of parameter to control secondary parton interactions [20], describe all of the data well (a  $\chi^2$  statistical test in Fig. 6 gives a value of 13.6 for a total of 18 data points). HERWIG describes the measured jet shapes well but produces jets slightly narrower than the data at low  $P_T^{\text{jet}}$ . This results in a significantly higher  $\chi^2$  value of 33.8 for 18 data points.

### B. Quark- and gluon-jet contributions

Figures 7 and 8 present the measured integrated jet shapes,  $\Psi(r/R)$ , as a function of  $P_T^{\text{jet}}$ , for jets with  $0.1 < |Y^{\text{jet}}| < 0.7$  and  $37 < P_T^{\text{jet}} < 380 \text{ GeV}$ , compared to PYTHIA-Tune A predictions (as in Figs. 4 and 5). In these figures predictions are also shown separately for quark- and gluon-jets. Each hadron-level jet from PYTHIA is classified as a quark- or gluon-jet by matching ( $Y$ - $\phi$  plane) its direction with that of one of the outgoing partons from the hard interaction. The Monte Carlo predictions indicate that, for the jets used in this analysis, the measured jet shapes are dominated by contributions from gluon-initiated jets at low  $P_T^{\text{jet}}$  while contributions from quark-initiated jets become important at high  $P_T^{\text{jet}}$ . This can be explained in terms of the different partonic contents in the proton and antiproton in the low- and high- $P_T^{\text{jet}}$  regions, since the mixture of gluon- and quark-jet in the final state partially reflects the nature of the incoming partons that participate in the hard interaction. Figure 9 shows the measured  $1 - \Psi(r_0/R)$ ,  $r_0 = 0.3$ , as a function of

$P_T^{\text{jet}}$  compared to PYTHIA-Tune A predictions with quark- and gluon-jets shown separately. For a given type of parton-jet in the Monte Carlo (quark- or gluon-jet), the observed trend with  $P_T^{\text{jet}}$  is partially due to the running of the strong coupling,  $\alpha_s(P_T^{\text{jet}})$ .

## IX. SUMMARY AND CONCLUSIONS

Jet shapes have been measured in inclusive jet production in  $p\bar{p}$  collisions for jets in the kinematic region  $37 \text{ GeV} < P_T^{\text{jet}} < 380 \text{ GeV}$  and  $0.1 < |Y^{\text{jet}}| < 0.7$ . Jets become narrower as  $P_T^{\text{jet}}$  increases, and the measured jet shapes show a strong dependence on the given gluon- and quark-jet content in the final state. PYTHIA Monte Carlo predictions, using default parameters, do not describe the measured jet shapes in the entire  $P_T^{\text{jet}}$  range. PYTHIA-Tune A, which includes enhanced contributions from initial-state gluon radiation and secondary parton interactions between remnants, describes the data. HERWIG gives a reasonable description of the measured jet shapes but tends to produce jets that are too narrow at low  $P_T^{\text{jet}}$  which can be attributed to the absent of soft contributions from multiple parton interactions in HERWIG. Jet shape measurements thus can be used to introduce strong constraints on phenomenological models describing soft-gluon radiation and the underlying event in hadron-hadron interactions.

## Acknowledgments

We thank the Fermilab staff and the technical staffs of the participating institutions for their vital contributions. This work was supported by the U.S. Department of Energy and National Science Foundation; the Italian Istituto Nazionale di Fisica Nucleare; the Ministry of Education, Culture, Sports, Science and Technology of Japan; the Natural Sciences and Engineering Research Council of Canada; the National Science Council of the Republic of China; the Swiss National Science Foundation; the A.P. Sloan Foundation; the Bundesministerium fuer Bildung und Forschung, Germany; the Korean Science and Engineering Foundation and the Korean Research Foundation; the Particle Physics and Astronomy Research Council and the Royal Society, UK; the Russian Foundation for Basic Research; the Comision Interministerial de Ciencia y Tecnologia, Spain; and in part by the European Community's Human Potential Programme under contract HPRN-CT-20002, Probe for New Physics.

- 
- [1] S.D.Ellis, Z. Kunszt and D.E. Soper, Phys. Rev. Lett. 69 (1992) 3615.
  - [2] CDF Collab., F. Abe et al., Phys. Rev. Lett. 70 (1993) 713.  
D0 Collab., S. Abachi et al., Phys. Lett. B357 (1995) 500.
  - [3] ZEUS Collab., J.Breitweg et al., The Eur. Phys. Journal C8 (1999) 3, 367-380.  
H1 Collab., C. Adloff et al., Nucl. Phys. B545 (1999) 3-20.
  - [4] ZEUS Collab., J.Breitweg et al., The Eur. Phys. Journal C2 (1998) 1, 61-75.
  - [5] OPAL Collab., R. Akers et al., Zeit. f. Phys. C63 (1994) 197.
  - [6] CDF II Collab., FERMILAB-PUB-96/390-E (1996).  
D. Acosta et al., Phys. Rev. D71, (2005) 032001.
  - [7] A. Sill et al., Nucl. Instrum. Meth. A447, (2000) 1.  
A. Affolder et al., Nucl. Instrum. Meth. A453, (2000) 84.  
C.S. Hill, Nucl. Instrum. Meth. A530, (2000) 1.
  - [8] T. Affolder et al., Nucl. Instrum. Meth. A526, (2004) 249.
  - [9] The pseudorapidity is defined as  $\eta = -\ln(\tan(\frac{\theta}{2}))$ , where the polar angle  $\theta$  is taken with respect to the proton beam direction. The rapidity is defined as  $Y = \frac{1}{2}\ln(\frac{E+p_z}{E-p_z})$ , where  $E$  denotes the energy and  $p_z$  is the component of the momentum along the proton beam direction.
  - [10] L. Balka et al., Nucl. Instr. Meth. A 267,(1988) 272.
  - [11] S. Bertolucci et al., Nucl. Instr. Meth. A 267, (1988) 301.
  - [12] R. Oishi, Nucl. Instr. Meth. A 453, (2000) 277.  
M. G. Albrow et al., Nucl. Instr. Meth. A 480, (2002) 524.
  - [13] D. Acosta et al., Nucl. Instrum. Meth., A494, 2002) 57.



- [14] B. L. Winer, Int. J. Mod. Phys. A A16S1C, (2001) 1169.
- [15] R. Brun, R. Hagelberg, M. Hansroul and J. C. Lassalle, CERN-DD-78-2-REV.  
S. Agostinelli et al., Nucl. Instrum. Meth. A 506, (2003) 250.
- [16] G. Grindhammer, M. Rudowicz and S. Peters, Nucl. Instrum. Meth. A 290 (1990) 469.
- [17] T. Sjöstrand et al., Comp. Phys. Comm. 135 (2001) 238 [hep-ph/0010017].
- [18] G. Corcella et al., JHEP 0101 (2001) 010 [hep-ph/0011363]; hep-ph/0210213.
- [19] J. Pumplin et al., JHEP 0207 (2002) 012.
- [20] PYTHIA-Tune A Monte Carlo samples are generated using the following tuned parameters in PYTHIA:  $\text{PARP}(67) = 4.0$ ,  $\text{MSTP}(82) = 4$ ,  $\text{PARP}(82) = 2.0$ ,  $\text{PARP}(84) = 0.4$ ,  $\text{PARP}(85) = 0.9$ ,  $\text{PARP}(86) = 0.95$ ,  $\text{PARP}(89) = 1800.0$ ,  $\text{PARP}(90) = 0.25$ .
- [21] D. Acosta et al., CDF Collaboration, Phys. Rev. D65, 092002, (2002).
- [22] B. Andersson et al., Phys. Rep. 97 (1983) 31.
- [23] T. Sjöstrand, Comp. Phys. Comm. 39 (1986) 347.
- [24] B.R. Webber, Nucl. Phys. B 238 (1984) 492.
- [25] G. C. Blazey, et al., hep-ex/0005012.  
S.D. Ellis, J. Huston and M. Toennesmann, hep-ph/0111434.
- [26] M. H. Seymour, Nucl.Phys. B513 (1998) 269-300.
- [27] CDF Collab., F. Abe et al., Phys. Rev. D45 (1992) 1448.
- [28] S.R. Hahn, et al., NIM A267, (1988) 351-366.
- [29] Olga Norniella, PhD. Thesis, Universitat Autònoma de Barcelona, in preparation.
- [30] Simon Sabik, PhD. Thesis, University of Toronto, in preparation.

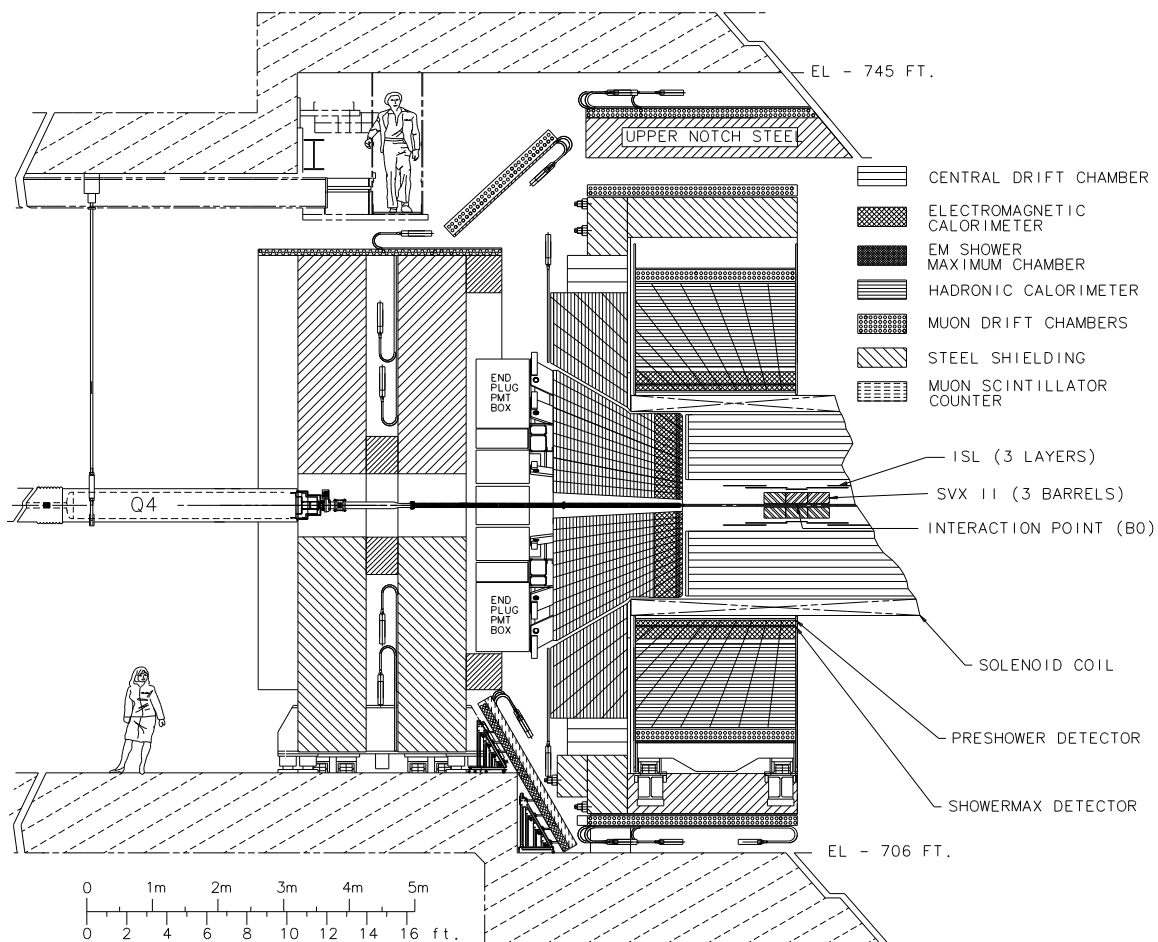


FIG. 1: Longitudinal view of half of the CDF II detector.

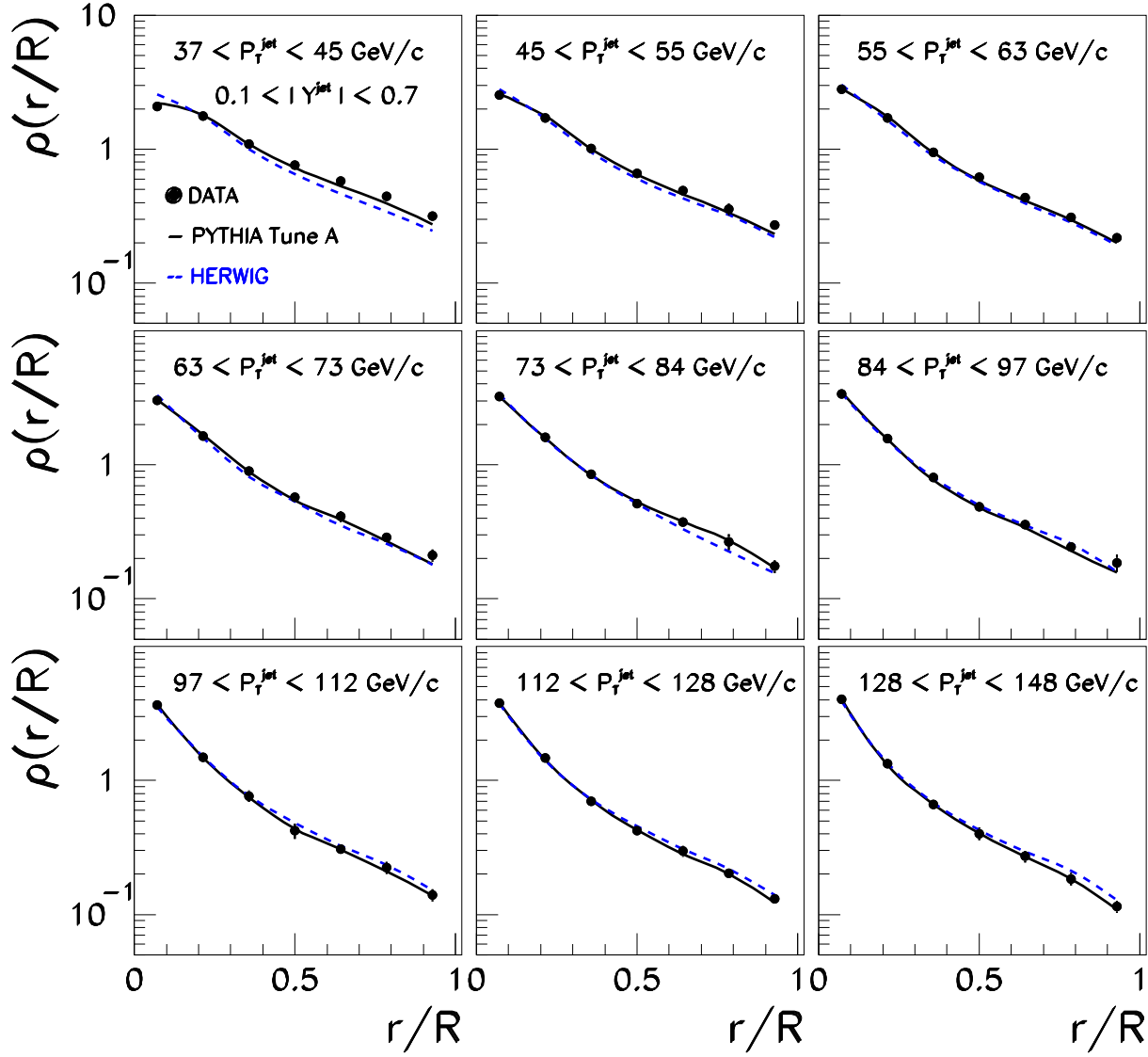


FIG. 2: The measured differential jet shape,  $\rho(r/R)$ , in inclusive jet production for jets with  $0.1 < |Y^{\text{jet}}| < 0.7$  and  $37 \text{ GeV} < P_T^{\text{jet}} < 148 \text{ GeV}$ , is shown in different  $P_T^{\text{jet}}$  regions. Error bars indicate the statistical and systematic uncertainties added in quadrature. The predictions of PYTHIA-Tune A (solid lines) and HERWIG (dashed lines) are shown for comparison.

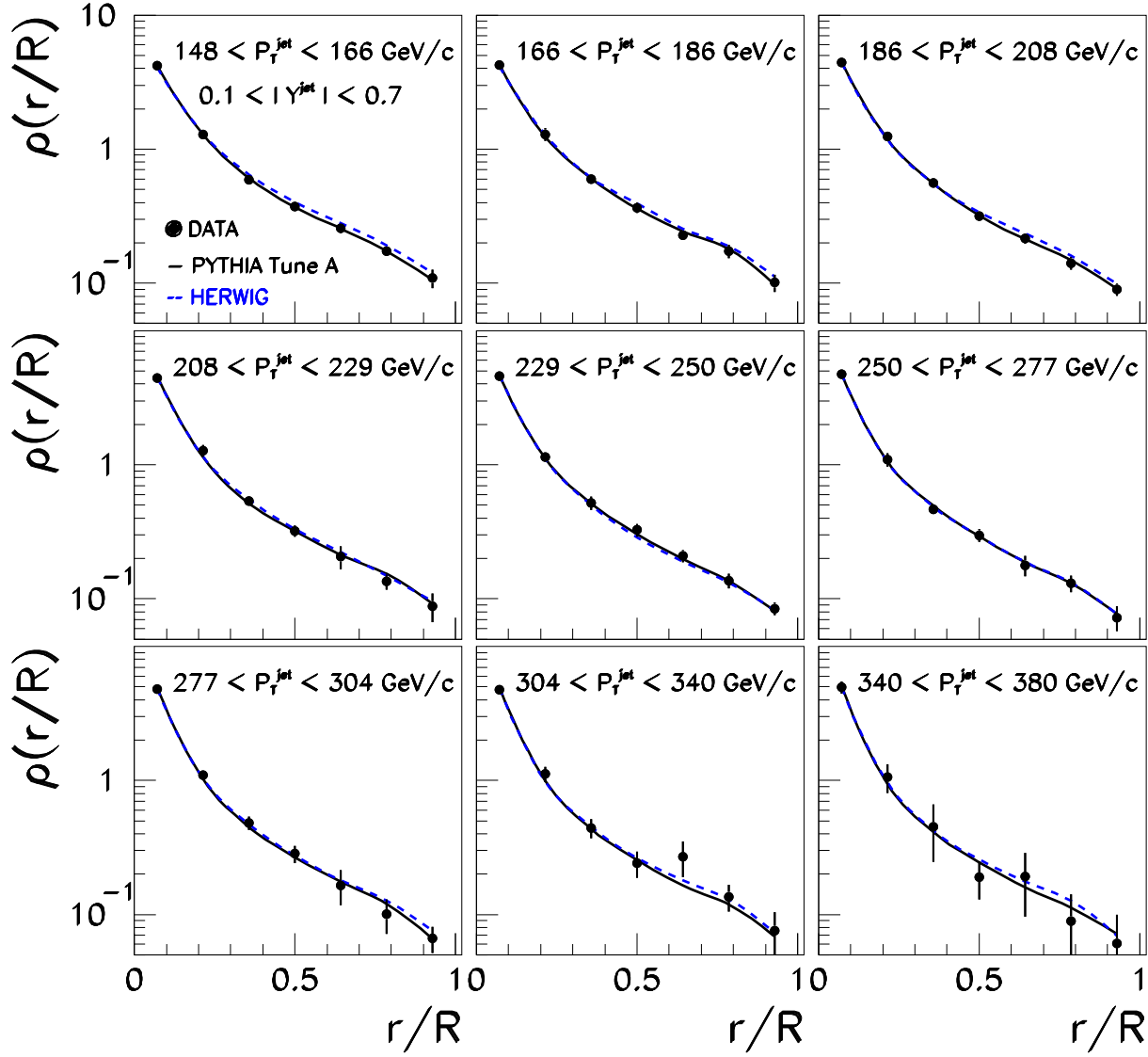


FIG. 3: The measured differential jet shape,  $\rho(r/R)$ , in inclusive jet production for jets with  $0.1 < |Y^{\text{jet}}| < 0.7$  and  $148 \text{ GeV} < P_T^{\text{jet}} < 380 \text{ GeV}$ , is shown in different  $P_T^{\text{jet}}$  regions. Error bars indicate the statistical and systematic uncertainties added in quadrature. The predictions of PYTHIA-Tune A (solid lines) and HERWIG (dashed lines) are shown for comparison.

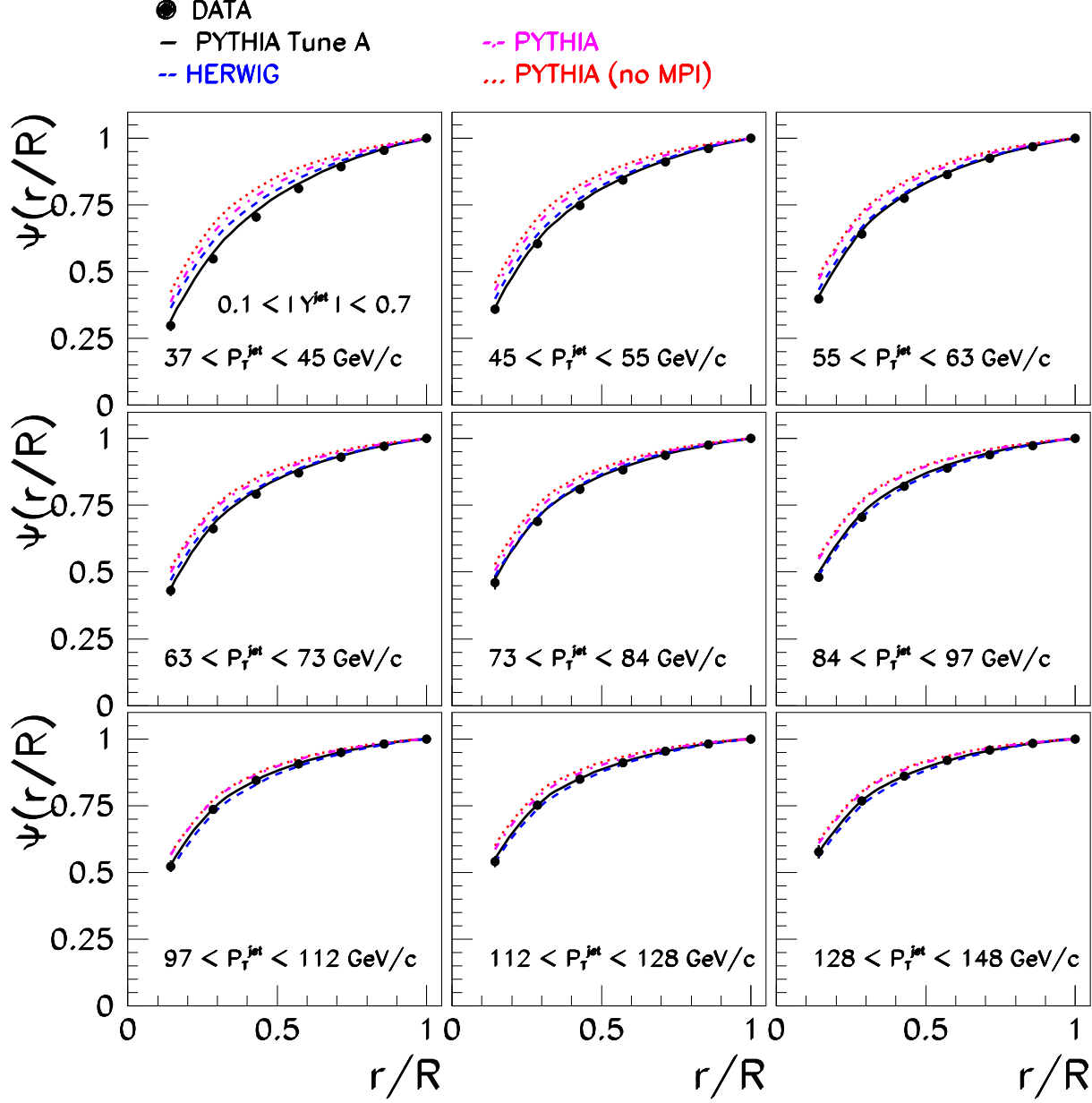


FIG. 4: The measured integrated jet shape,  $\Psi(r/R)$ , in inclusive jet production for jets with  $0.1 < |Y^{\text{jet}}| < 0.7$  and  $37 \text{ GeV} < P_T^{\text{jet}} < 148 \text{ GeV}$ , is shown in different  $P_T^{\text{jet}}$  regions. Error bars indicate the statistical and systematic uncertainties added in quadrature. The predictions of PYTHIA-Tune A (solid lines), PYTHIA (dashed-dotted lines), PYTHIA-(no MPI) (dotted lines) and HERWIG (dashed lines) are shown for comparison.

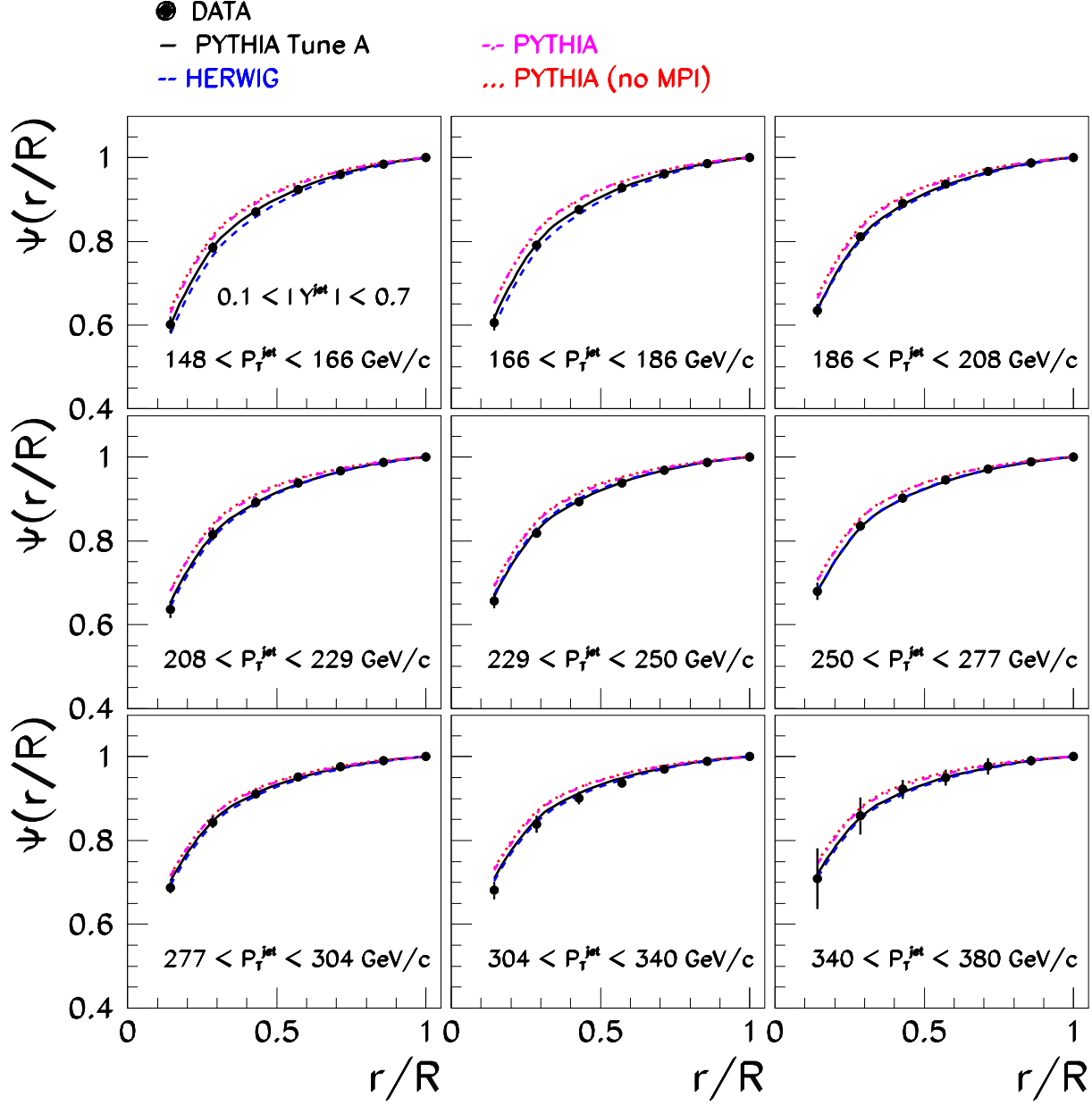


FIG. 5: The measured integrated jet shape,  $\Psi(r/R)$ , in inclusive jet production for jets with  $0.1 < |Y^{\text{jet}}| < 0.7$  and  $148 \text{ GeV} < P_T^{\text{jet}} < 380 \text{ GeV}$ , is shown in different  $P_T^{\text{jet}}$  regions. Error bars indicate the statistical and systematic uncertainties added in quadrature. The predictions of PYTHIA-Tune A (solid lines), PYTHIA (dashed-dotted lines), PYTHIA-(no MPI) (dotted lines) and HERWIG (dashed lines) are shown for comparison.

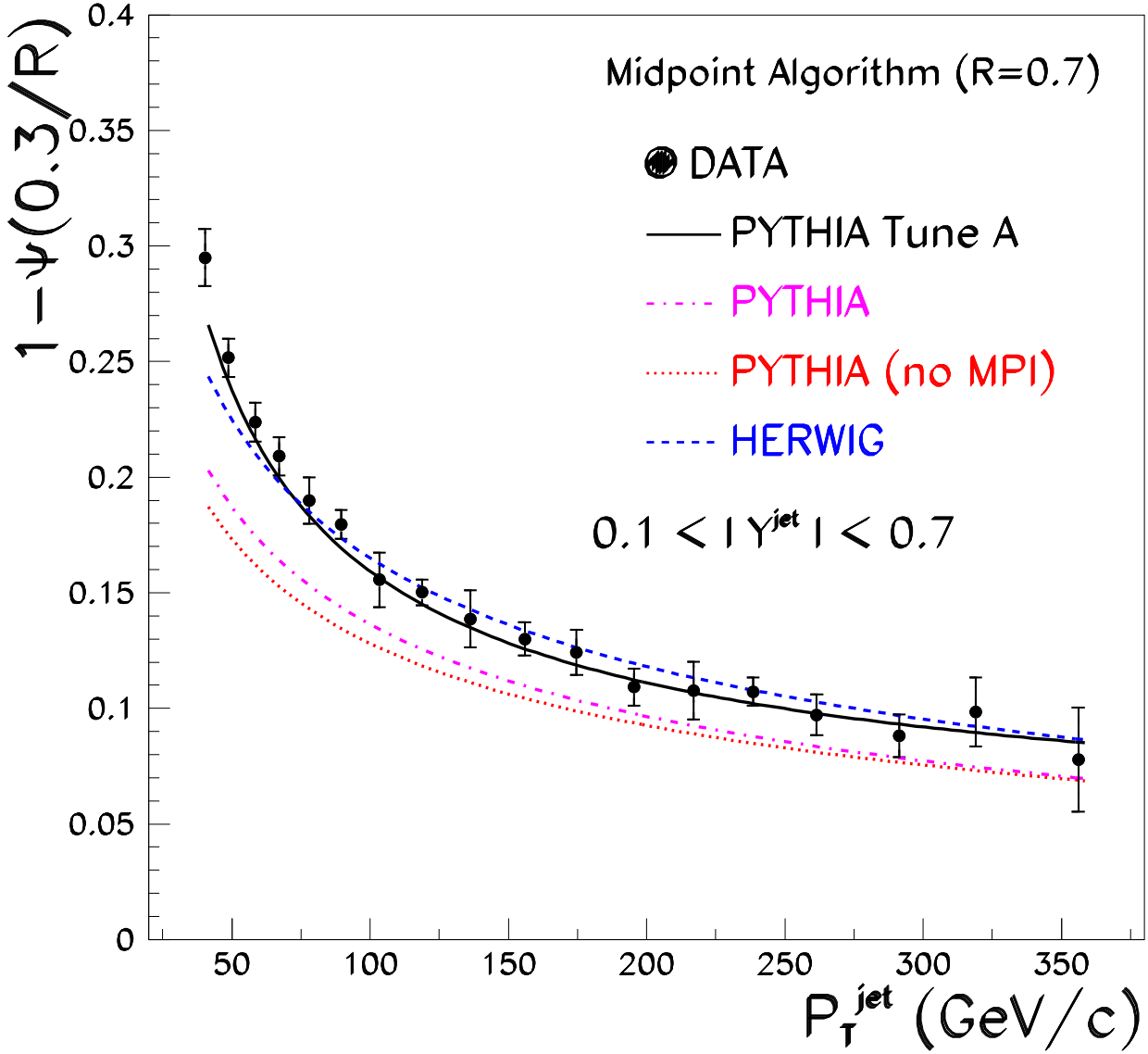


FIG. 6: The measured  $1 - \Psi(0.3/R)$  as a function of  $P_T^{\text{jet}}$  for jets with  $0.1 < |Y^{\text{jet}}| < 0.7$  and  $37 \text{ GeV} < P_T^{\text{jet}} < 380 \text{ GeV}$ . Error bars indicate the statistical and systematic uncertainties added in quadrature. The predictions of PYTHIA-Tune A (solid line), PYTHIA (dashed-dotted line), PYTHIA-(no MPI) (dotted line) and HERWIG (dashed line) are shown for comparison.

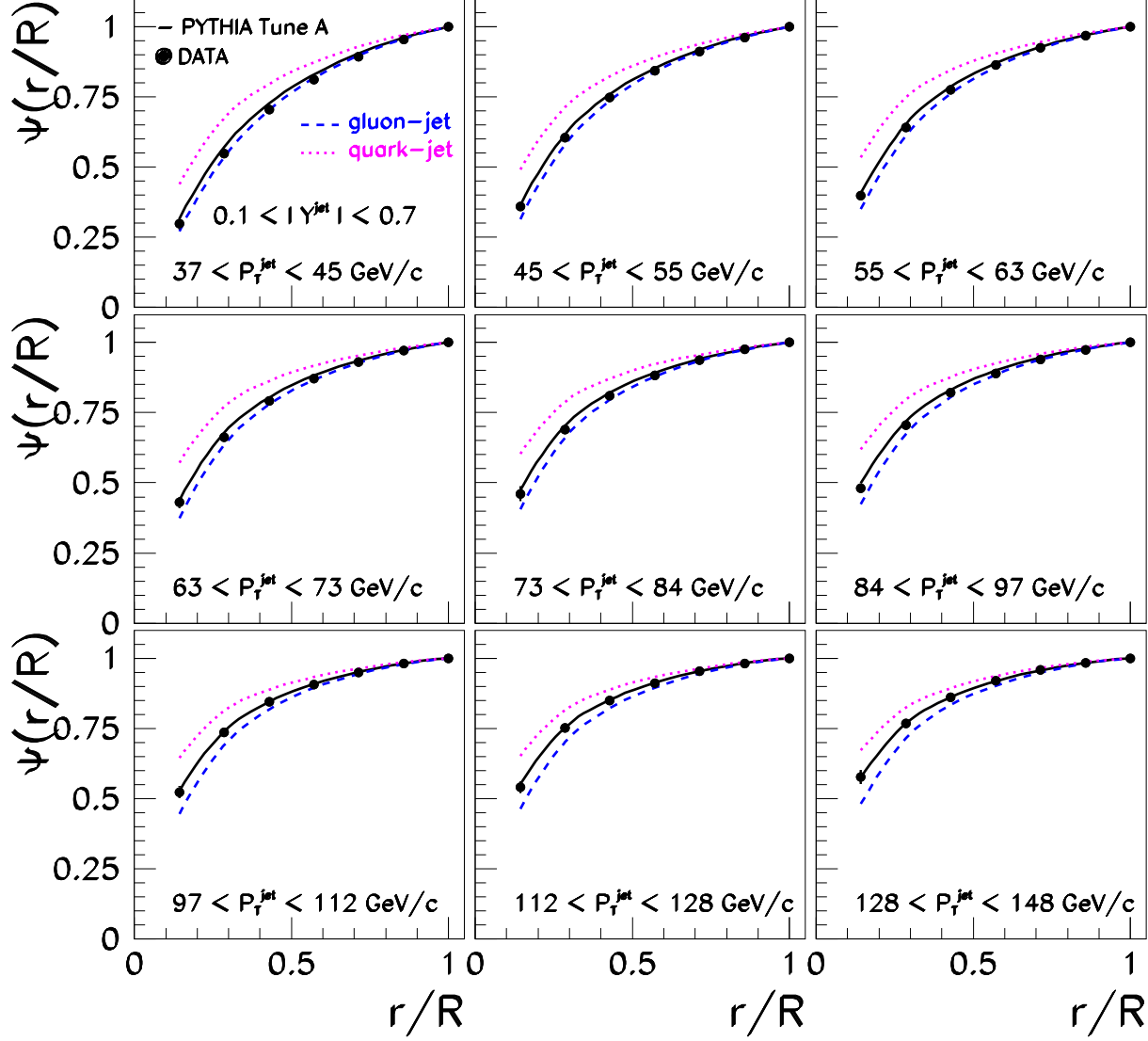


FIG. 7: The measured integrated jet shape,  $\Psi(r/R)$ , in inclusive jet production for jets with  $0.1 < |Y^{\text{jet}}| < 0.7$  and  $37 \text{ GeV} < P_T^{\text{jet}} < 148 \text{ GeV}$ , is shown in different  $P_T^{\text{jet}}$  regions. Error bars indicate the statistical and systematic uncertainties added in quadrature. The predictions of PYTHIA-Tune A (solid lines) and the separate predictions for quark-initiated jets (dotted lines) and gluon-initiated jets (dashed lines) are shown for comparison.



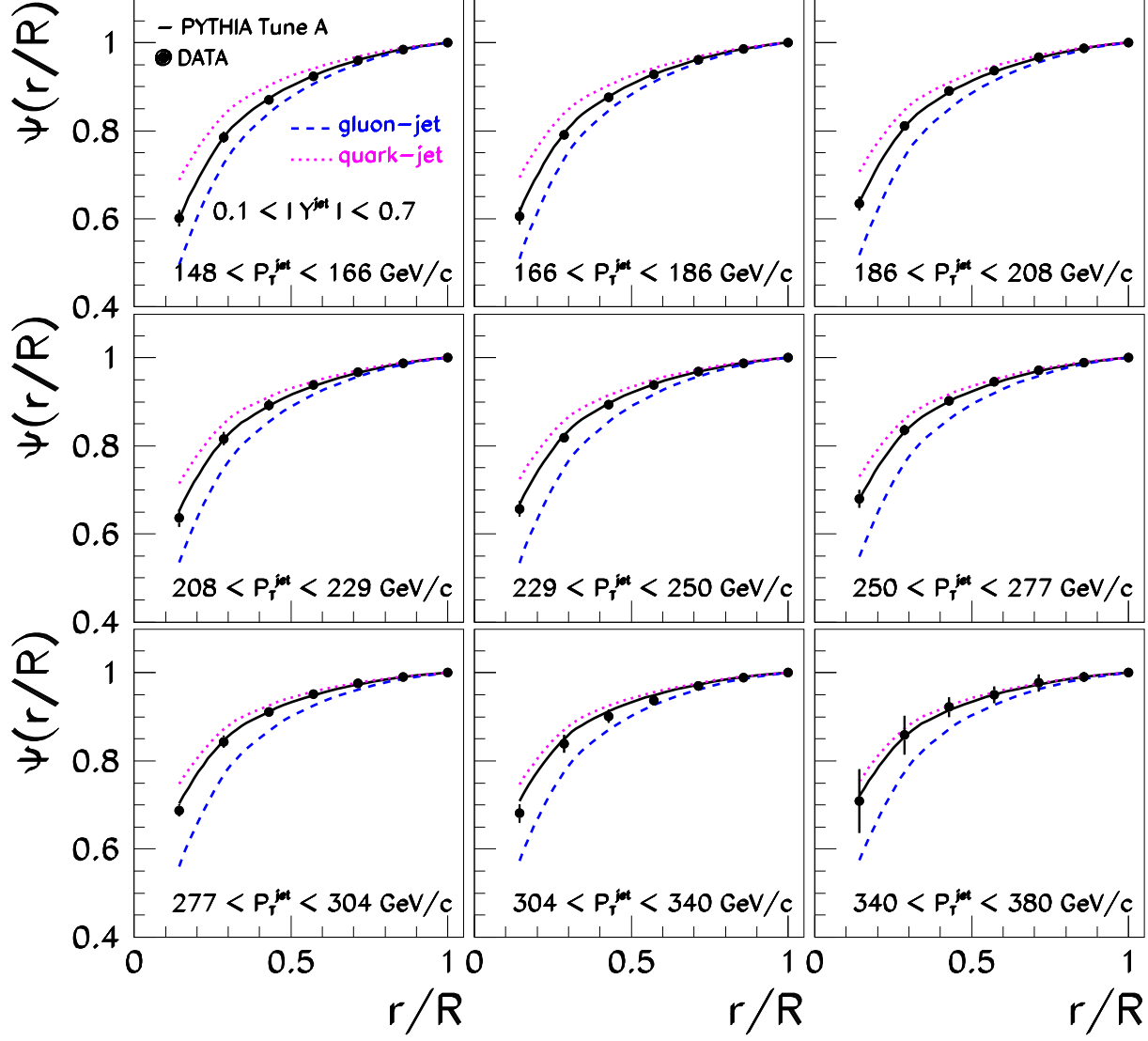


FIG. 8: The measured integrated jet shape,  $\Psi(r/R)$ , in inclusive jet production for jets with  $0.1 < |Y^{\text{jet}}| < 0.7$  and  $148 \text{ GeV} < P_T^{\text{jet}} < 380 \text{ GeV}$ , is shown in different  $P_T^{\text{jet}}$  regions. Error bars indicate the statistical and systematic uncertainties added in quadrature. The predictions of PYTHIA-Tune A (solid lines) and the separate predictions for quark-initiated jets (dotted lines) and gluon-initiated jets (dashed lines) are shown for comparison.

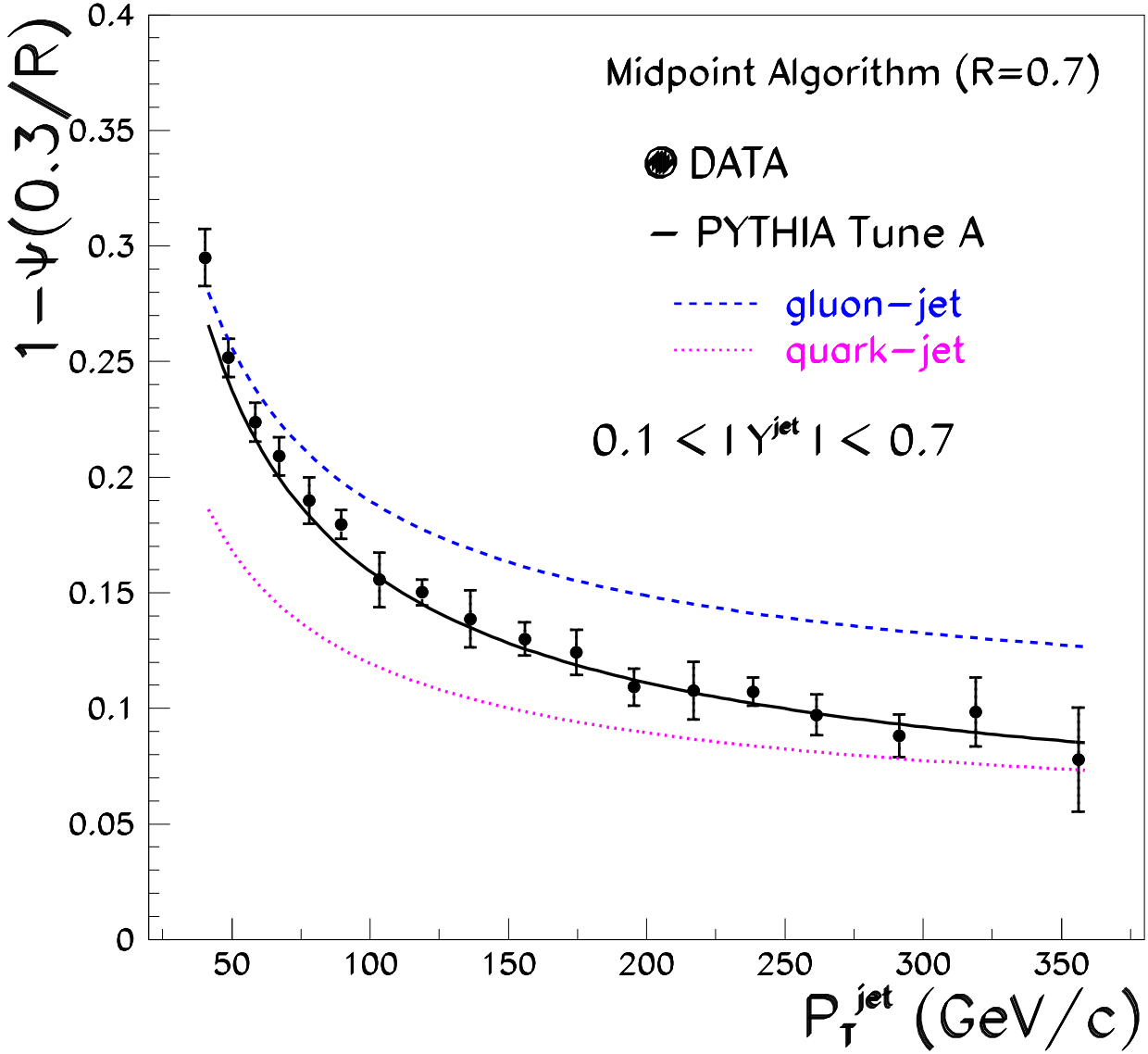


FIG. 9: The measured  $1 - \Psi(0.3/R)$  as a function of  $P_T^{\text{jet}}$  for jets with  $0.1 < |Y^{\text{jet}}| < 0.7$  and  $37 \text{ GeV} < P_T^{\text{jet}} < 380 \text{ GeV}$ . Error bars indicate the statistical and systematic uncertainties added in quadrature. The predictions of PYTHIA-Tune A (solid line) and the separate predictions for quark-initiated jets (dotted line) and gluon-initiated jets (dashed line) are shown for comparison.